coatings

MDPI

Article

Influences of SiO_2 Additions on the Structures and Thermal Properties of $AlTaO_4$ Ceramics as EBC Materials

Bingyan Wu [1,2], Luyang Zhang [1,2], Lin Chen [1,2,*], Jiankun Wang [1,2], Zipeng Gao [1,2] and Jing Feng [1,2,*]

[1] Faculty of Materials Science and Engineering, Kunming University of Science and Technology, Kunming 650093, China
[2] National-Local Joint Engineering Laboratory for Technology of Advanced Metallic Solidification Forming and Equipment, Kunming 650093, China
* Correspondence: chenlin_mater@kust.edu.cn (L.C.); jingfeng@kust.edu.cn (J.F.)

Abstract

Ceramic matrix composites (CMCs) are extensively utilized in aero engines due to their high-temperature stability; however, they are prone to environmental corrosion at high temperatures, and environmental barrier coatings (EBCs) are necessary to resist oxidation and corrosion. Among various EBC materials, $AlTaO_4$ offers high cost-effectiveness and low thermal expansion coefficients (TECs), but its resistance to SiO_2 erosion and high-temperature stability remain unclear. We investigated the influences of SiO_2 additions on the structures and thermal properties of $AlTaO_4$; and $AlTaO_4$ mixtures containing 10 wt.% SiO_2 were kept at 1400 °C for 30–120 h. $AlTaO_4$ exhibited excellent high-temperature phase stability, and SiO_2 dissolved into $AlTaO_4$ to generate a solid solution. XRD Rietveld refinement was employed to confirm the position of Si in the lattices, while SEM and EDS characterizations demonstrated the homogeneous distribution of Si, Al, and Ta elements. At 1200 °C, the TECs of SiO_2-$AlTaO_4$ (4.65×10^{-6} K^{-1}) were close to those of SiC ($4.5–5.5 \times 10^{-6}$ K^{-1}). Additionally, the addition of SiO_2 could reduce TECs of $AlTaO_4$, a feature that helped alleviate the interface thermal stress between $AlTaO_4$ and the Si bond coat in the EBC systems. At 900 °C, the thermal conductivity was reduced by 26.9% compared to that of $AlTaO_4$, and the lowest value was 1.65 $W \cdot m^{-1} \cdot K^{-1}$. Accordingly, SiO_2 will enter the lattices of $AlTaO_4$ after heat treatments at 1400 °C, and SiO_2 additions will reduce the thermal conductivity and TECs of $AlTaO_4$, which is beneficial for its EBC applications.

Keywords: EBCs; thermal conductivity; thermal expansion; SiO_2 chemical compatibility

check for updates

Academic Editor: Hyung-Ho Park

Received: 4 September 2025
Revised: 6 October 2025
Accepted: 10 October 2025
Published: 13 October 2025

Citation: Wu, B.; Zhang, L.; Chen, L.; Wang, J.; Gao, Z.; Feng, J. Influences of SiO_2 Additions on the Structures and Thermal Properties of $AlTaO_4$ Ceramics as EBC Materials. *Coatings* **2025**, *15*, 1204. https://doi.org/10.3390/coatings15101204

Copyright: © 2025 by the authors. Licensee MDPI, Basel, Switzerland. This article is an open access article distributed under the terms and conditions of the Creative Commons Attribution (CC BY) license (https://creativecommons.org/licenses/by/4.0/).

1. Introduction

With the continuous developments in aero engine technology, the turbine inlet temperature of advanced aero engines has risen to 1600 °C, which exceeds the melting points of high-temperature nickel-based alloys [1–3]. Ceramic matrix composites (CMCs) exhibit excellent high-temperature stability and can withstand long-term exposure to temperatures of up to 1600 °C, leading to their performance being significantly superior to that of nickel-based alloys [4–7]. The applications of CMCs can effectively enhance engine thermal efficiency and reduce cooling air demand. Using CMCs to manufacture engine turbine components can reduce the weight by 50%–67%, which significantly lowers engine weight and further improves aircraft fuel efficiency [8]. For example, SiC fiber-reinforced SiC (SiC_f/SiC) composites have a density of approximately 2 $g \cdot cm^{-3}$, which is much less than that of high-temperature alloys [3,9–14]. Some CMCs can achieve twice the strength

of nickel-based alloys and combine high specific strength and specific modulus. Therefore, CMCs can withstand high stress and maintain good mechanical properties in the harsh engine environment.

In the actual operating conditions of gas turbine engines, CMCs operate in air at temperatures exceeding 1200 °C, where they react with environmental dust (primarily calcium-magnesium-alumino-silicate (CMAS) [15–18], fuel impurities, and high-temperature water vapor, and a SiO_2 passivation layer is formed [19]. The dense SiO_2 layer is capable of inhibiting the further oxidation of both the Si bond coat and the CMCs. However, high-temperature steam induces further corrosion of SiO_2, resulting in the formation of volatile $Si(OH)_4$ and subsequent degradation of CMCs [20]. To address this issue, environmental barrier coatings (EBCs) are applied to the CMC's surface to isolate high-temperature corrosive media [21–23].

EBCs should exhibit low thermal conductivity for protecting the substrate; match the thermal expansion coefficients (TECs) of the CMCs to avoid coating cracking at high temperatures [24,25]; possess a high melting point to ensure operations in high-temperature environments; and exhibit resistance to erosion by CMAS and high-temperature water vapor [26,27]. Current EBC candidates include aluminates [28,29], phosphates [30–32], hafnates [33,34], zirconates [35–38], tantalates [39–41], and niobates [42–46]. However, each of these material systems has inherent drawbacks that restrict their applications [47–50]. Among various materials, $AlTaO_4$ is regarded as a promising EBC material, attributed to its excellent thermal stability, low thermal expansion coefficients (TECs), and superior mechanical properties [51]. According to the selling prices on the official website of Aladdin Reagents as of 3 October 2025, 100 g of Al_2O_3 costs RMB 142.90, but commonly used rare earth oxides, such as 100 g of Sm_2O_3, are priced at RMB 2829.90, and 100 g of Sc_2O_3 is priced at RMB 2758.90. From an economic perspective, $AlTaO_4$ demonstrates significant advantages compared to $RETaO_4$ during the synthesis process [52]. Since the Si bond coat reacts continuously with oxygen in the environment during long-term service in high-temperature environments, a thermally grown oxide (TGO: SiO_2) layer is gradually formed. The stability, densification, and bonding state with the top coating of this TGO layer directly affect the protective lifespan of the entire coating system [53–57]. Therefore, it is particularly critical to evaluate the interfacial interaction between $AlTaO_4$ and the SiO_2 derived from the Si bond coat. Specifically, two key aspects need to be considered: first, whether the presence of SiO_2 will form a second phase with $AlTaO_4$ (which may lead to performance failure), and second, whether the difference in thermal expansion coefficients between SiO_2 and $AlTaO_4$ EBCs will affect the structural integrity of $AlTaO_4$ during service. The chemical compatibility between the two ultimately determines the service performance of $AlTaO_4$ EBCs under high temperatures.

Thus, this study focuses on 1400 °C (a typical high-temperature service range) and systematically investigates the chemical reaction behavior between $AlTaO_4$ and SiO_2 at this temperature. It further evaluates the effects of SiO_2 introduction and prolonged high-temperature environments on the applicability of $AlTaO_4$ as EBCs in high-temperature service scenarios, providing an experimental basis for the subsequent composition design and process optimization of $AlTaO_4$ EBCs.

2. Materials and Methods

2.1. Synthesis of Materials

The pristine powders of Ta_2O_5 (purity > 99.9%, particle size $\leq$ 30 μm, Macklin, Shanghai, China) and Al_2O_3 (purity > 99.9%, particle size $\leq$ 30 μm, Macklin, China) were mixed in a stoichiometric ratio and homogenized via wet planetary ball milling at a rotational speed of 300 r/min for a duration of 12 h. The homogenized slurry was dried in

an oven at approximately 70 °C for 24 h. After complete drying, the resultant powder was sintered in a tube furnace under ambient air atmosphere at 1500 °C for a holding time of 6 h. Subsequently, the sintered powder was removed, ground, and sieved through a 300-mesh screen to obtain the pristine $AlTaO_4$ powder (purity > 99.9%, particle size $\leq$ 50 μm).

The $AlTaO_4$ powder and SiO_2 powder (purity > 99.9%, particle size $\leq$ 30 μm, Macklin, China) were weighed at a mass ratio of 9:1 and homogenized via wet planetary ball milling at a rotational speed of 300 r/min for a duration of 12 h. The homogenized slurry was dried in an oven at approximately 70 °C for 24 h. Upon complete drying, the resultant powder was uniaxially pressed into disc-shaped green bodies with a height of 2 mm and a radius of 7.5 mm under a pressure of 320 MPa. These green discs were then sintered in a tube furnace under ambient air atmosphere at 1400 °C for holding times of 30, 60, 90, and 120 h, respectively. In the present study, the samples corresponding to the aforementioned sintering times were designated as the 30 h, 60 h, 90 h, and 120 h samples, respectively. The bulk density of the prepared samples was measured using the Archimedes method, and the porosity (φ) was calculated by comparing the measured bulk density with the theoretical density.

2.2. Structural Identification

Phase characterization of the sintered samples was conducted using an X-ray diffractometer (XRD, MiniFlex 600, Rigaku, Tokyo, Japan), and subsequent Rietveld refinement of the obtained XRD patterns was performed via the General Structure Analysis System (GSAS-II, SVN version 5455) software to quantify phase composition. For microstructural and elemental analysis, a scanning electron microscope (SEM, JSM-7800F, JEOL, Tokyo, Japan) equipped with an energy-dispersive spectrometer (EDS, 6751A-6UUS-SN, Thermo Scientific, Waltham, MA, USA) was employed to observe grain size, surface pores, and elemental distribution. The Raman spectrum was measured using a laser confocal Raman microscope (LABRAM Soleil, HORIBA, Palaiseau, France) with an excitation wavelength of 532 nm, over the range of 50–1100 cm^{-1}.

2.3. Measurements of Thermal Properties

The TECs of the samples were measured using a dilatometer (DIL 402, NETZSCH, Selb, Germany) at a heating rate of 5 °C/min. For thermal diffusivity (α) testing, a laser flash apparatus (LFA457, NETZSCH, Germany) was employed, with the measurement conducted at a heating rate of 10 °C/min. The thermal diffusivity was determined using the Radiation Pulse correction model available in the system, with a deviation of less than 2%. Three independent measurements were conducted at each point. Due to the extremely small test error, no explanation was provided in this paper. The thermal conductivity (k) was further calculated via Equation (1), using the experimentally obtained thermal diffusivity, density (ρ), and specific heat (Cp) [58].

$$k = \alpha \cdot \rho \cdot C_p \quad (1)$$

3. Results and Discussion

3.1. Crystal Structure

Figure 1a shows the XRD patterns of $AlTaO_4$ and SiO_2 mixtures after heat treatment at 1400 °C for various durations. The peaks of each sample matched well with the standard card of $AlTaO_4$ (PDF#01-076-0363), which had a monoclinic phase and space group C2/m.

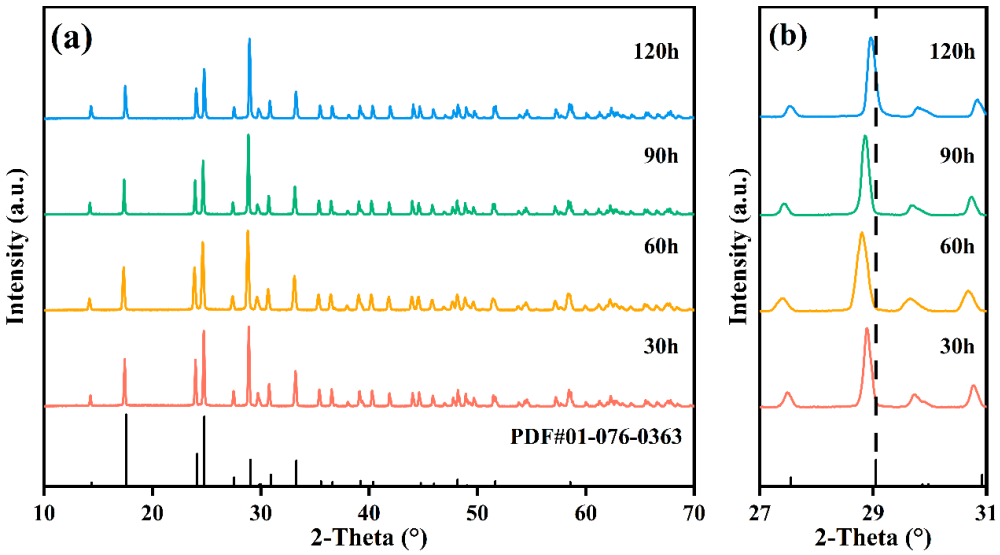


Figure 1. XRD patterns of SiO_2-$AlTaO_4$ ceramics. (**a**) 2-Theta = 10–70°; (**b**) 2-Theta = 27–31°.

The ionic radii of Al^{3+}, Si^{4+}, and Ta^{5+} were 50, 42, and 69 pm [59], respectively. The difference in ionic radii between Al^{3+} and Si^{4+}, calculated via Equation (2), was 16%, and that between Ta^{5+} and Si^{4+} was 39.13%. XRD results indicated that SiO_2 had dissolved into the $AlTaO_4$ lattice to form a SiO_2-$AlTaO_4$ solid solution.

$$\Delta r = \frac{r_1 - r_2}{r_1} \quad (2)$$

In Figure 1b, a shift in characteristic peaks was observed. The main peaks after heat treatment for 30–60 h showed a progressive left shift, while those heat-treated for 90–120 h gradually shifted to the right compared with the sample heated for 60 h. According to Bragg's equation, an increase in interplanar spacing (d) gave rise to a reduction in diffraction angle (2θ), and this resulted in a left shift in the diffraction peaks. After 120 h of heat treatment, the opposite process might have occurred. The above phenomenon was presumably caused by the position of Si in the $AlTaO_4$ lattice, which was influenced by heat treatment time. The *sig* and R_{wp} values in Figure 2 indicated high confidence in the XRD refinement results.

Table 1 presents the changes in lattice constants, unit cell volume, theoretical density, and porosity. The refinement results were consistent with those reported in previous work [51].

Table 1. Lattice constants and theoretical density (ρ) of SiO_2-$AlTaO_4$ ceramics obtained from the XRD Rietveld refinements.

Sample	a (Å)	b (Å)	c (Å)	β (°)	V (Å^3)	ρ (g·cm^{-3})	Porosity
30 h	12.135	3.776	6.449	107.730	281.469	6.238	30.3%
60 h	12.136	3.779	6.449	107.710	281.747	6.232	36.1%
90 h	12.135	3.777	6.449	107.720	281.559	6.236	39.7%
120 h	12.148	3.766	6.458	107.705	281.455	6.238	38.9%

Specifically, for samples heat-treated for 30–60 h, the unit cell volume was expanded, and the theoretical density was decreased. For the samples heat-treated for 90–120 h, the unit cell volume began to shrink, and the theoretical density increased compared to the samples heat-treated for 30–60 h. The above results indicate that the heat treatment

time indeed caused changes in the position of Si atoms in the $AlTaO_4$ lattice. Si occupied interstitial sites in $AlTaO_4$ after heat treatment for 30–60 h, and an interstitial solid solution was formed, resulting in lattice expansion. After 60–90 h heat treatment, the lattice thermal vibrations of $AlTaO_4$ were further intensified to increase atomic spacing and expand interstitial sizes. Si atoms moved from interstitial sites to lattice sites, and a substitutional solid solution was triggered to reduce the unit cell volume. Figure 3 shows the crystal structure of $AlTaO_4$ when Si occupies both the Ta and Al atomic sites. In the lattices of $AlTaO_4$, Al and Ta atoms were bonded to six O atoms, and Si atoms had a probability of 5% to occupy the sites of Al and Ta atoms. The polyhedron distortion (Δd) was calculated using Equation (3) [60,61]:

$$\Delta d = \frac{1}{n}\sum_{n}\left[\frac{L-\bar{L}}{\bar{L}}\right]^2 \quad (3)$$

where L represents the bond length of A–O (A = Al, Ta), $\bar{L}$ represents the average bond length of [AlO_6] and [TaO_6], and n represents the number of bonds as illustrated in Figure 3.

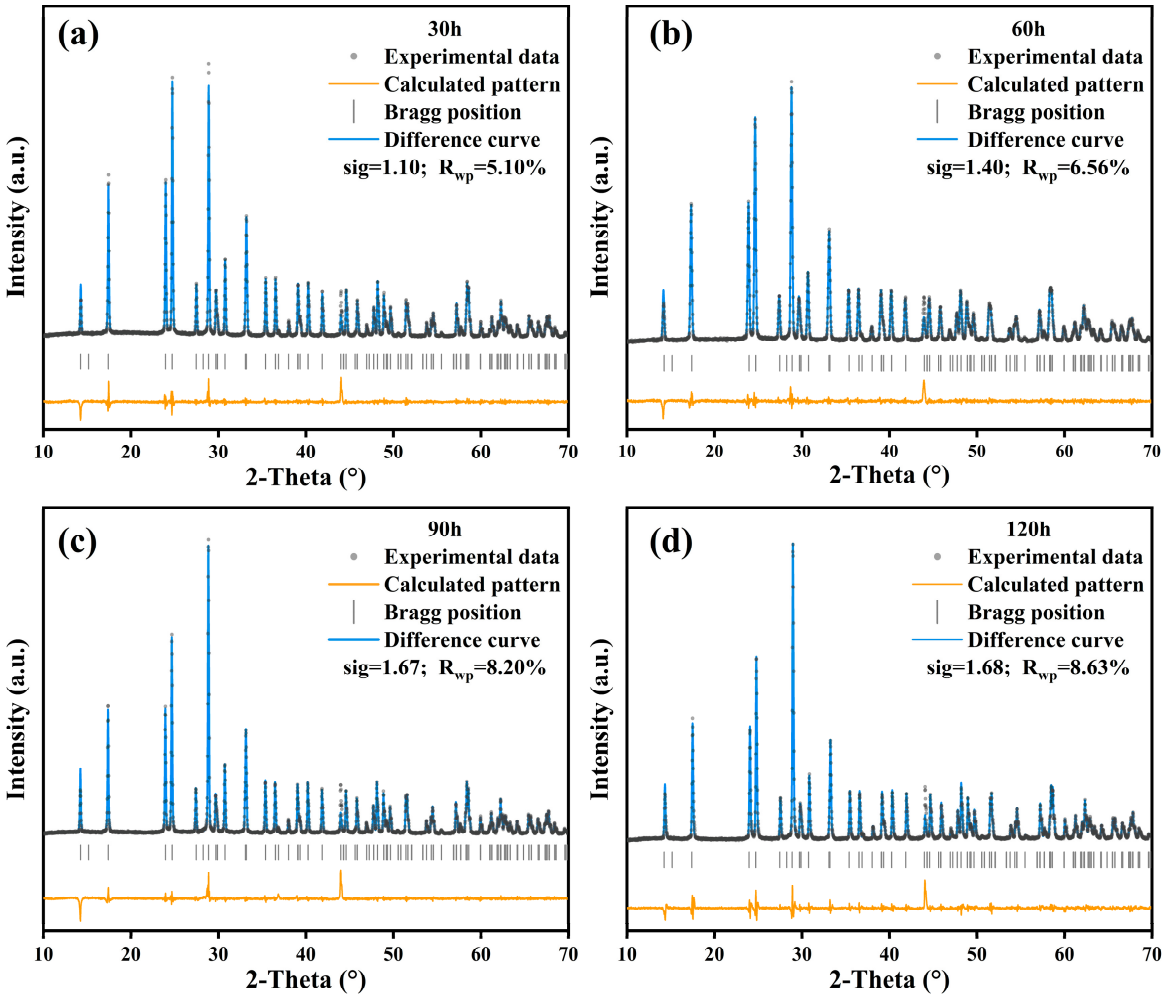


Figure 2. The XRD Rietveld refinements of SiO_2-$AlTaO_4$. (**a**) 30 h; (**b**) 60 h; (**c**) 90 h; and (**d**) 120 h.

The results are shown in Figure 4. The total distortion index showed a trend of increasing and then decreasing, which was consistent with the XRD refinement results. The distortion was dominated by the Al-O bonds, and this was consistent with the changes in the position of Si.

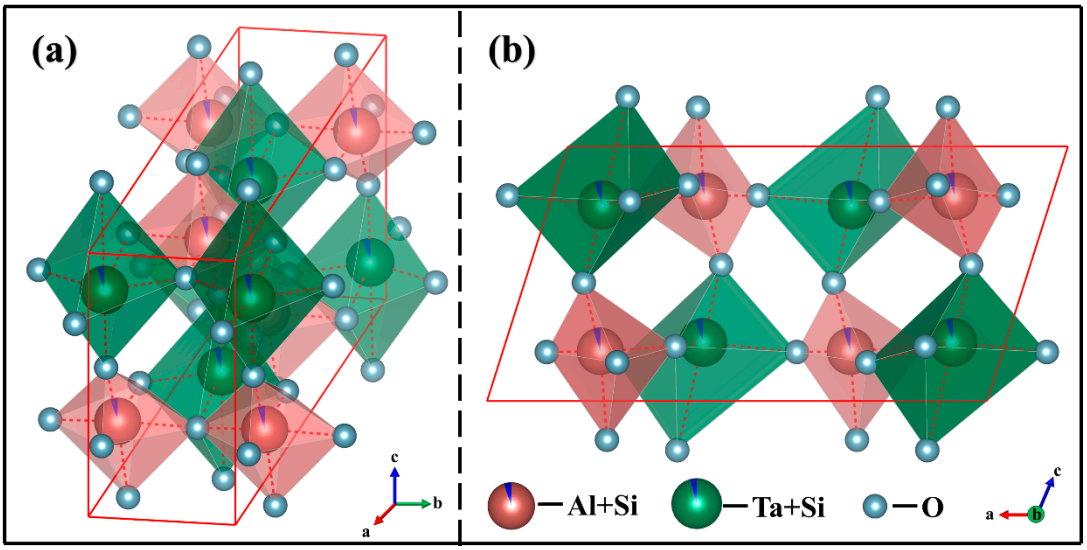


Figure 3. Crystal structures of SiO_2-$AlTaO_4$ ceramics. (**a**) Three-dimensional structure; (**b**) Viewing along the *b* axis.

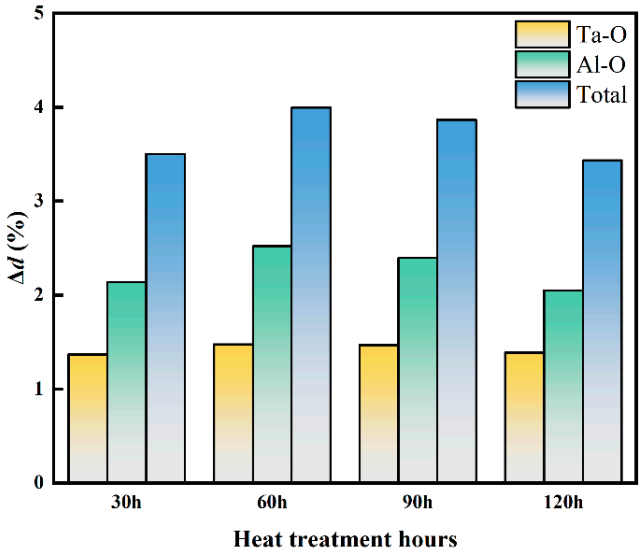


Figure 4. The distortion degree of polyhedra in lattices of SiO_2-$AlTaO_4$ ceramics obtained from the XRD refinement.

3.2. Microstructures and Elemental Distributions

Figure 5 shows the surface morphology of SiO_2-$AlTaO_4$ and the corresponding EDS mapping for samples heat-treated for different durations, and it illustrates the changes in grain size and surface morphology. It can be denoted that the grain size of SiO_2-$AlTaO_4$ ceramics after heat treatment for different durations ranged from submicron to micron scale. As the heat treatment time increased, the grains gradually grew and arranged more regularly, and the sample heat-treated for 120 h had the largest grains.

EDS mapping revealed the homogeneous distribution of Si, Al, Ta, and O elements within the grains without obvious segregation, and the microstructure of SiO_2-$AlTaO_4$ remained largely unaffected by SiO_2 addition and heat treatment duration. Figure 6 showed the atomic ratio of each element based on the EDS spectra, which was consistent with the experimental design.

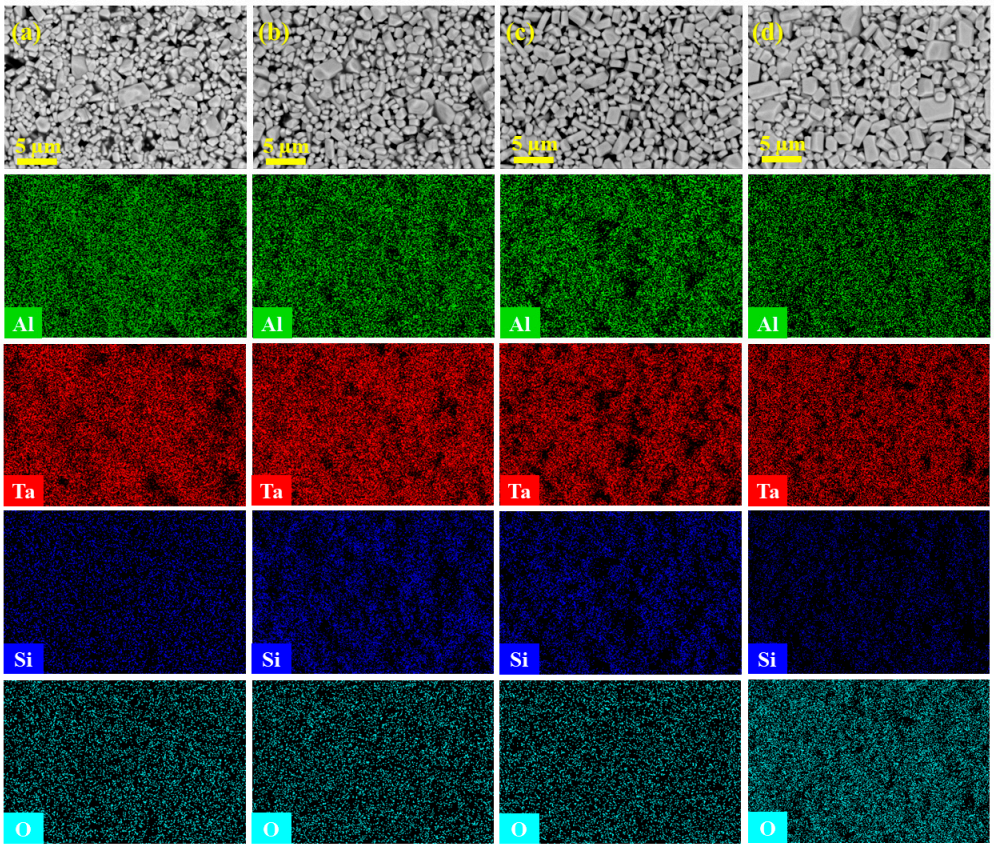


Figure 5. Typical microstructures and EDS mapping of SiO_2-$AlTaO_4$ after different heat treatment times: (**a**) 30 h; (**b**) 60 h; (**c**) 90 h; and (**d**) 120 h.

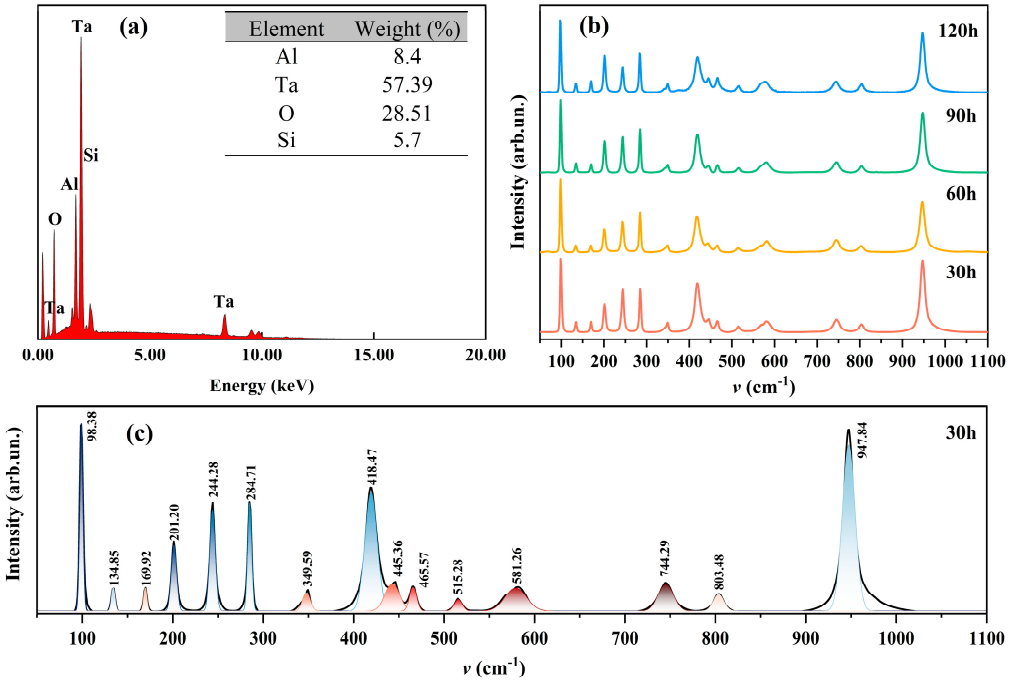


Figure 6. (**a**) EDS spectra of SiO_2-$AlTaO_4$ after heat treatment at 1400 °C for 30 h; (**b**) Raman spectra from 50 to 1100 cm^{-1} for each sample; and (**c**) The fitted Raman spectrum of the 30 h.

3.3. Raman Spectra

The Raman spectrum of SiO_2-$AlTaO_4$ is shown in Figure 6b. Obviously, the characteristic peak positions in the Raman spectra of all samples maintained good consistency, indi-

cating that the core structure of the samples remained unchanged during the 30–120 h heat treatment process, with only slight changes in peak intensity and peak shape. Raman spectrum correction was performed on the 30 h sample, and the results are shown in Figure 6c. The peaks at wavenumbers of 98.38, 134.85, 169.92, 201.20, 244.28, and 284.71 cm^{-1} corresponded to the characteristic peaks of the Al-Ta-O framework. The peaks at 349.59, 418.47, 445.36, 515.28, and 581.26 cm^{-1} mostly corresponded to Ta-O bonds or Al-O bonds. The strong peak at 947.84 cm^{-1} was a characteristic identification peak of $AlTaO_4$, corresponding to the characteristic stretching vibration of [TaO_6] octahedrons [62,63]. The appearance of the weak peak at 465.57 cm^{-1} confirmed the existence of Si-O bonds. The above results indicated that there was no second-phase SiO_2 in SiO_2-$AlTaO_4$.

3.4. Thermal Properties

Based on the above results, a solid solution phase was formed after heat treatments. Therefore, it was important to evaluate changes in the thermal properties of SiO_2-$AlTaO_4$. Figure 7a showed a comparison of thermal expansion rates between SiO_2-$AlTaO_4$, $AlTaO_4$, and $AlNbO_4$ [51]. The results showed that the slopes of the thermal expansion rate curves remained stable as the temperature increased, which indicated good high-temperature stability. The thermal expansion rate of SiO_2-$AlTaO_4$ was significantly lower than that of $AlTaO_4$ and $AlNbO_4$. Mechanistically, thermal expansion essentially resulted from the increase in average atomic distance due to intensified atomic thermal vibrations. Figure 7b showed their TECs, which had a positive correlation with temperature.

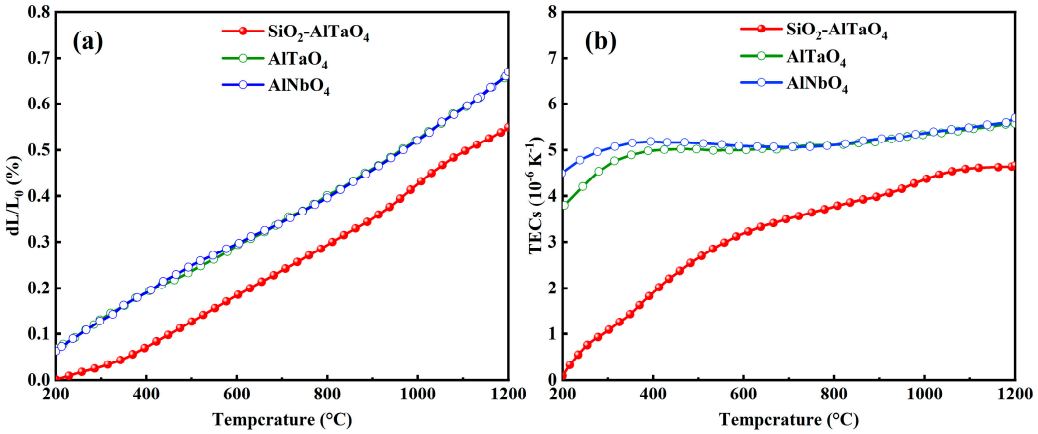


Figure 7. Thermal expansion performance of SiO_2-$AlTaO_4$, $AlTaO_4$, and $AlNbO_4$ ceramics [51]: (**a**) Thermal expansion rate; (**b**) TECs.

The TECs of SiO_2-$AlTaO_4$ increased rapidly initially and gradually stabilized at temperatures beyond 1100 °C and reached approximately 4.65 × 10^{-6} K^{-1} at 1200 °C, which were close to the TECs of SiC (4.5–5.5 × 10^{-6} K^{-1}) [4,64]. The TECs of SiO_2-$AlTaO_4$ were significantly lower than those of $AlTaO_4$ and $AlNbO_4$, which could be attributed to the following reasons. (i) After SiO_2 and $AlTaO_4$ formed a solid solution, Si ions were introduced into the $AlTaO_4$ lattices, which caused the lattice distortion and micro-local stress. The stress restrained atomic thermal vibrations and made it difficult for atoms to expand freely as the temperature increased, thereby reducing the TECs [65,66]. (ii) The reduced lattice distortion decreased the vibrational entropy to improve lattice order and enhanced the bonding strength among different atoms, which further reduced TECs [67]. (iii) The SiO_2-$AlTaO_4$ ceramics had porosities of 30%–40%, which were much higher than the porosities of $AlTaO_4$ and $AlNbO_4$ reported in Ref. [51], and a high porosity would decrease TECs. Obviously, the SiO_2 would react with $AlTaO_4$ to form a solid solution, and

the TECs were decreased at the same time, which was good for reducing the interface thermal stress between $AlTaO_4$ and the bond coat in the EBC system.

The low thermal conductivity of EBCs can provide high thermal insulation for CMCs, thereby extending their service life. Figure 8a showed the thermal diffusivity of SiO_2-$AlTaO_4$, which ranged from 1.39 to 0.60 $mm^2 \cdot s^{-1}$ at 25–900 °C. Compared to $AlTaO_4$, SiO_2-$AlTaO_4$ had a lower thermal diffusivity below 400 °C, and they had similar thermal diffusivity at 400–900 °C. Also, SiO_2-$AlTaO_4$ had a lower thermal diffusivity than $AlNbO_4$, $Yb_2Si_2O_7$, and other EBC materials [51,68,69]. Figure 8b compared the thermal conductivity of SiO_2-$AlTaO_4$ with other oxides [51,68–71]; and their thermal conductivity showed a decreasing trend with the increasing temperature, which was consistent with the behavior of insulating materials.

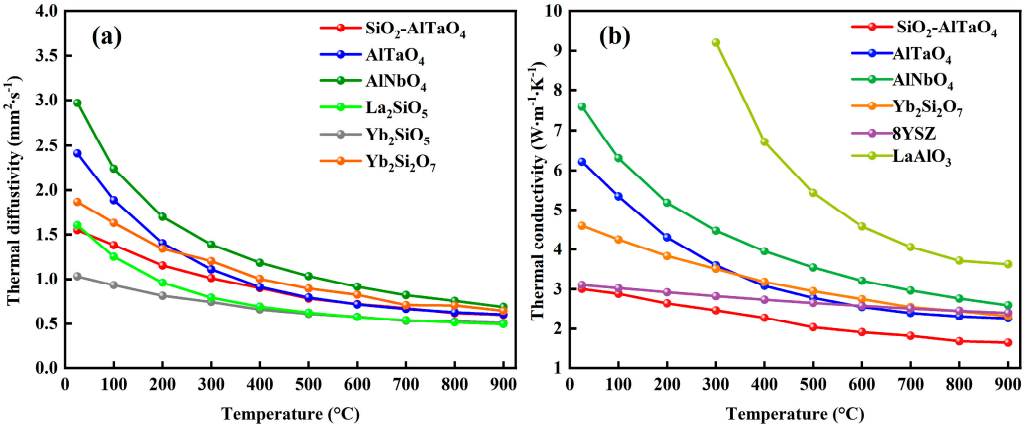


Figure 8. Thermal properties of SiO_2-$AlTaO_4$ and other oxides [51,68–71]: (**a**) Thermal diffusivities; (**b**) Thermal conductivities.

As the temperature increased, the atomic thermal vibrations intensified, and phonon scattering was enhanced, resulting in a decrease in thermal conductivity. The thermal conductivity of SiO_2-$AlTaO_4$ exhibited a decreasing trend with increasing temperature, ranging from 2.91 to 1.65 $W \cdot m^{-1} \cdot K^{-1}$ at temperatures between 25 °C and 900 °C. It could be seen that the thermal conductivity of SiO_2-$AlTaO_4$ was significantly lower than that of $AlTaO_4$. At 900 °C, $AlTaO_4$ exhibited a thermal conductivity of 2.26 $W \cdot m^{-1} \cdot K^{-1}$, whereas the thermal conductivity of SiO_2-$AlTaO_4$ was only 1.65 $W \cdot m^{-1} \cdot K^{-1}$; obviously, the introduction of SiO_2 led to a 26.9% reduction in the thermal conductivity of $AlTaO_4$. Compared to other oxides, SiO_2-$AlTaO_4$ ceramics exhibited a low thermal conductivity, and SiO_2 addition enhanced the phonon scattering in $AlTaO_4$.

4. Conclusions

This study investigated the high-temperature reaction behaviors between SiO_2 and $AlTaO_4$, and the influences of SiO_2 additions on thermal conductivity and TECs were studied. The conclusions were:

(1) The SiO_2-$AlTaO_4$ samples heat-treated at 1400 °C for 30–120 h maintained the monoclinic phase, and Si occupied the interstitial sites to form an interstitial solid solution at 30–60 h, where the Si atom migrated to lattice sites to form a substitutional solid solution at 90–120 h. $AlTaO_4$ exhibited excellent high-temperature stability, and the addition of SiO_2 did not alter its crystal structure.

(2) SEM and EDS mapping revealed the uniform distribution of Si, Al, Ta, and O elements in each sample, without obvious segregation. The grain sizes were on the micron scale, gradually increasing in size and becoming more regularly arranged with extended

heat treatment time. The XRD, SEM, and EDS results synergistically indicated the good phase stability of $AlTaO_4$.

(3) The TECs of SiO_2-$AlTaO_4$ were approximately 4.65 × 10^{-6} K^{-1} at 1200 °C, which were lower than those of $AlTaO_4$ and $AlNbO_4$. The SiO_2 additions could reduce the TECs of $AlTaO_4$, thereby reducing the thermal stress between $AlTaO_4$ and the Si bond coat. The thermal conductivity at 900 °C was 26.9% lower than that of $AlTaO_4$, and the lowest value reached 1.65 $W{\cdot}m^{-1}{\cdot}K^{-1}$ as the phonon scattering strength was increased. Accordingly, the reaction between SiO_2 and $AlTaO_4$ could reduce the TECs and thermal conductivity, which were good for the EBC applications.

Author Contributions: Methodology, L.Z., L.C. and J.W.; Validation, B.W.; Investigation, B.W. and Z.G.; Data curation, B.W.; Writing—original draft, B.W.; Writing—review & editing, B.W., L.C. and J.F.; Supervision, L.Z., L.C., J.W. and J.F.; Project administration, L.C. and J.F. All authors have read and agreed to the published version of the manuscript.

Funding: Thanks for the support from the National Natural Science Foundation (Nos. 52562006 and 52502065), National Key Research and Development Program of China (No. 2022YFB3708600), Yunnan Fundamental Research Projects (No. 202201BE070001-008), General Project in Yunnan Province (Nos. 202201AT070192 and 202101BE070001-011), and Open Project of Yunnan Precious Metals Laboratory (No. 2023050240).

Institutional Review Board Statement: Not applicable.

Informed Consent Statement: Not applicable.

Data Availability Statement: The data presented in this study are available on request from thecorresponding author due to legal.

Conflicts of Interest: The authors declare that they have no known competing financial interests or personal relationships that could have appeared to influence the work reported in this paper.

References

1. Shin, S.; Wang, Q.Y.; Luo, J.; Chen, R.K. Advanced materials for high-temperature thermal transport. *Adv. Funct. Mater.* **2020**, *30*, 1904815. [CrossRef]
2. George, E.P.; Raabe, D.; Ritchie, R.O. High-entropy alloys. *Nat. Rev. Mater.* **2019**, *4*, 515–534. [CrossRef]
3. Chen, L.; Li, B.H.; Feng, J. Rare-earth tantalates for next-generation thermal barrier coatings. *Prog. Mater Sci.* **2024**, *144*, 101265. [CrossRef]
4. Lee, K.N. Current status of environmental barrier coatings for Si-Based ceramics. *Surf. Coat. Technol.* **2000**, *133–134*, 1–7. [CrossRef]
5. Chen, S.Y.; Chen, Z.K.; Wang, J.M.; Zeng, Y.; Song, W.L.; Xiong, X.; Li, X.C.; Li, T.Q.; Wang, Y.C. Insight into the effect of Ti substitutions on the static oxidation behavior of (Hf,Ti)C at 2500 °C. *Adv. Powder Mater.* **2024**, *3*, 100168. [CrossRef]
6. Sciti, D.; Vinci, A.; Zoli, L.; Galizia, P.; Failla, S.; Mungiguerra, S.; Di Martino, G.D.; Cecere, A.; Savino, R. Propulsion tests on ultra-high-temperature ceramic matrix composites for reusable rocket nozzles. *J. Adv. Ceram.* **2023**, *12*, 1345–1360.
7. Guo, L.X.; Huang, S.W.; Li, W.; Lv, J.S.; Sun, J. Theoretical design and experimental verification of high-entropy carbide ablative resistant coating. *Adv. Powder Mater.* **2024**, *3*, 100213. [CrossRef]
8. He, X.; Yuan, X.H.; Xu, H.; Song, P.; Yu, X.; Li, C.; Huang, T.H.; Li, Q.L.; Lü, K.Y.; Feng, J.; et al. Analysis of structure and microhardness of Al_2O_3-40 wt.% TiO_2/NiCoCrAl gradient coating with in-situ needle-like phase reinforcement after high-temperature treatment. *Ceram. Int.* **2019**, *45*, 14546–14554. [CrossRef]
9. Madar, R. Silicon carbide in contention. *Nature* **2004**, *430*, 974–975. [CrossRef] [PubMed]
10. Kedir, N.; Garcia, E.; Kirk, C.; Gao, J.L.; Guo, Z.R.; Zhai, X.D.; Sun, T.; Fezzaa, K.; Sampath, S.; Chen, W.W. Impact damage of narrow silicon carbide (SiC) ceramics with and without environmental barrier coatings (EBCs) by various foreign object debris (FOD) simulants. *Surf. Coat. Technol.* **2021**, *407*, 126779. [CrossRef]
11. Zou, B.L.; Khan, Z.S.; Fan, X.Z.; Huang, W.Z.; Gu, L.J.; Wang, Y.; Xu, J.Y.; Tao, S.Y.; Yang, K.Y.; Ma, H.M.; et al. A new double layer oxidation resistant coating based on Er_2SiO_5/$LaMgAl_{11}O_{19}$ deposited on C/SiC composites by atmospheric plasma spraying. *Surf. Coat. Technol.* **2013**, *219*, 101–108.
12. Zhang, S.C.; Wu, L.H.; Sun, X.K.; Sun, H.R.; Ai, B.; Chen, Y.F. Ultra-low thermal conductivity multilayer composites for insulation in low pressure environments. *Adv. Ceram.* **2023**, *44*, 442–450.

13. Liu, X.F.; He, J.F.; Li, Y.G.; Li, H.; Lei, W.; Jia, Q.L.; Zhang, S.W.; Zhang, H.J. Foam-gelcasting preparation of porous SiC ceramic for high-temperature thermal insulation and infrared stealth. *Rare Met.* **2023**, *42*, 3829–3838.
14. Zhang, J.X.; Zhang, J.; Ye, X.L.; Ma, X.M.; Liu, R.; Sun, Q.L.; Zhou, Y.L. Ultralight and compressive SiC nanowires aerogel for high-temperature thermal insulation. *Rare Met.* **2023**, *42*, 3354–3363.
15. Wright, A.J.; Mock, C.; Sharobem, T.; Sotiropoulos, N.; Dambra, C.; Keyes, B.; Ghoshal, A. Integrated microstructural and chemical approach for improving CMAS resistance in thermal and environmental barrier coatings. *Coatings* **2025**, *15*, 680. [CrossRef]
16. Wu, Y.; Guo, X.; He, D.Y. Research progress of CMAS corrosion and protection method for thermal barrier coatings in aero-engines. *China Surf. Eng.* **2023**, *36*, 1–13.
17. Bryce, K.; Majee, B.P.; Huang, L.P.; Lian, J. A systematic study of thermomechanical properties and calcium-magnesium-aluminosilicate (CMAS) corrosion of multicomponent rare-earth phosphates. *J. Adv. Ceram.* **2024**, *13*, 1807–1822.
18. Zhang, L.Y.; Luo, K.R.; Chen, L.; Wang, J.K.; Li, B.H.; Feng, J. $A_4Ta_2O_9$ (A = Ca, Mg) tantalate as novel thermal barrier coatings materials with superior calcium-magnesium-alumino-silicate corrosion resistance. *J. Eur. Ceram. Soc.* **2025**, *45*, 117090. [CrossRef]
19. Naraparaju, R.; Schulz, U.; Mechnich, P.; Döbber, P.; Seidel, F. Degradation study of 7wt.% yttria stabilised zirconia (7YSZ) thermal barrier coatings on aero-engine combustion chamber parts due to infiltration by different CaO-MgO-Al_2O_3-SiO_2 variants. *Surf. Coat. Technol.* **2014**, *260*, 73–81. [CrossRef]
20. Niu, Z.B.; Li, D.X.; Jia, D.C.; Yang, Z.H.; Lin, K.P.; Riedel, R.; Colombo, P.; Zhou, Y. Oxidation behavior of amorphous and nanocrystalline SiBCN ceramics—Kinetic consideration and microstructure. *Adv. Powder Mater.* **2024**, *3*, 100163. [CrossRef]
21. Richards, B.T.; Wadley, H.N.G. Plasma spray deposition of tri-layer environmental barrier coatings. *J. Eur. Ceram. Soc.* **2014**, *34*, 3069–3083. [CrossRef]
22. An, K.; Wang, Y.Q.; Sui, Y.; Qing, Y.Q.; Tong, W.; Wang, X.Z.; Liu, C.S. Recent advances of cerium compounds in functional coatings: Principle, strategies and applications. *J. Rare Earths* **2025**, *43*, 227–245. [CrossRef]
23. Xie, Y.S.; Peng, Y.; Deng, Z.Z.; Zhu, Z.; Cheng, Y.; Ma, D.H.; Zhu, L.Y.; Zhang, X.H. Synergistic regulation of temperature resistance and thermal insulation performance of zirconia-based ceramic fibers. *Rare Met.* **2023**, *42*, 4189–4200. [CrossRef]
24. Yang, D.L.; Liu, J.L.; Zhang, J.G.; Liang, X.H.; Zhang, X.F. In situ high-Temperature tensile fracture mechanism of PS-PVD EBCs. *Coatings* **2022**, *12*, 655. [CrossRef]
25. Deijkers, J.A.; Wadley, H.N.G. A duplex bond coat approach to environmental barrier coating systems. *Acta Mater.* **2021**, *217*, 117167. [CrossRef]
26. Cao, G.; Wang, S.Q.; Ding, Z.Y.; Wang, Y.H.; Liu, Z.G.; Ouyang, J.H.; Wang, Y.M.; Wang, Y.J. High temperature corrosion behavior and the inhibition of apatite formation evolving from corrosion of $(Y_{1-x}Yb_x)_2SiO_5$ in water vapor environment. *Appl. Surf. Sci.* **2022**, *601*, 154284.
27. Dong, S.J.; Lü, K.Y.; Wang, Y.H.; Zeng, J.Y.; Yuan, J.Y.; Jiang, J.N.; Deng, L.H.; Cao, X.Q. High-temperature corrosion of $HfSiO_4$ environmental barrier coatings exposed to water vapor/oxygen atmosphere and molten calcium magnesium aluminosilicate. *Corros. Sci.* **2022**, *197*, 110081.
28. Xiang, H.M.; Feng, Z.H.; Li, Z.P.; Zhou, Y.C. Crystal structure, mechanical and thermal properties of $Yb_4Al_2O_9$: A combination of experimental and theoretical investigations. *J. Eur. Ceram. Soc.* **2017**, *37*, 2491–2499. [CrossRef]
29. Morán-Ruiz, A.; Vidal, K.; Larrañaga, A.; Arriortua, M.I. Characterization of $Ln_4Al_2O_9$ (Ln = Y, Sm, Eu, Gd, Tb) rare-earth aluminates as novel high-temperature barrier materials. *Ceram. Int.* **2018**, *44*, 8761–8767. [CrossRef]
30. Bryce, K.; Shih, Y.-T.; Huang, L.; Lian, J. Calcium-magnesium-aluminosilicate (CMAS) corrosion resistance of high entropy rare-earth phosphate $(Lu_{0.2}Yb_{0.2}Er_{0.2}Y_{0.2}Gd_{0.2})PO_4$: A novel environmental barrier coating candidate. *J. Eur. Ceram. Soc.* **2023**, *43*, 6461–6472. [CrossRef]
31. Zhang, P.X.; Wang, E.H.; Guo, C.Y.; Yang, T.; Hou, X.M. High-entropy rare earth phosphates ($REPO_4$, RE = Ho, Tm, Yb, Lu, Dy, Er and Y) with excellent comprehensive properties. *J. Eur. Ceram. Soc.* **2024**, *44*, 1873–1879. [CrossRef]
32. Karaulov, A.G.; Zoz, E.I. Phase formation in the ZrO_2-HfO_2-Gd_2O_3 and ZrO_2-HfO_2-Yb_2O_3 systems. *Refract. Ind. Ceram* **1999**, *40*, 479–483. [CrossRef]
33. Mikuśkiewicz, M.; Migas, D.; Moskal, G. Synthesis and thermal properties of zirconate, hafnate and cerate of samarium. *Surf. Coat. Technol.* **2018**, *354*, 66–75. [CrossRef]
34. Lopato, L.M.; Red'Ko, V.P.; Gerasimyuk, G.I.; Shevchenko, A.V. ChemInform abstract: Synthesis and properties of the compounds $M_4Zr_3O_{12}$ and $M_4Hf_3O_{12}$ (M: Rare earth element). *ChemInform* **1991**, *22*. [CrossRef]
35. Mikuśkiewicz, M.; Moskal, G.; Stopyra, M.; Korol, J. Thermal diffusivity and conductivity of Pr, Eu and Ho zirconates. *J. Therm. Anal. Calorim.* **2025**, *150*, 1195–1204. [CrossRef]
36. Chen, Q.; Xu, J.; Wang, H.C.; Wu, J.Z.; Dong, H.; Zhai, B.X.; He, J.; Gao, F. Thermophysical properties of Yb^{3+}-doped nonstoichiometric gadolinium zirconate ceramics. *Ceram. Int.* **2024**, *50*, 47813–47823. [CrossRef]
37. Fan, Y.; Bai, Y.L.; Li, Q.; Lu, Z.Y.; Chen, D.; Liu, Y.C.; Li, W.X.; Liu, B. Compositional design and phase formation capability of high-entropy rare-earth disilicates from machine learning and decision fusion. *npj Comput. Mater.* **2024**, *10*, 95. [CrossRef]

38. Herweyer, L.A.; Opila, E.J. High-temperature Na_2SO_4 interaction with air plasma sprayed $Yb_2Si_2O_7$ + Si EBC system: Topcoat behavior. *J. Am. Ceram. Soc.* **2021**, *104*, 6496–6507. [CrossRef]
39. Chen, L.; Hu, M.Y.; Wu, P.; Feng, J. Thermal expansion performance and intrinsic lattice thermal conductivity of ferroelastic $RETaO_4$ ceramics. *J. Am. Ceram. Soc.* **2019**, *102*, 4809–4821. [CrossRef]
40. Ogawa, T.; Matsudaira, T.; Yokoe, D.; Kawai, E.; Kawashima, N.; Fisher, C.A.J.; Habu, Y.; Kato, T.; Kitaoka, S. Spontaneously formed nanostructures in double perovskite rare-earth tantalates for thermal barrier coatings. *Acta Mater.* **2021**, *216*, 117152. [CrossRef]
41. Chen, L.; Hu, M.Y.; Zheng, X.D.; Feng, J. Characteristics of ferroelastic domains and thermal transport limits in HfO_2 alloying $YTaO_4$ ceramics. *Acta Mater.* **2023**, *251*, 118870. [CrossRef]
42. Tian, L.J.; Peng, F.; Song, X.M.; Zheng, W.; Liu, Z.W.; Huang, Y.L.; Zeng, Y. Enhancing the thermodynamic properties of rare-earth niobates through high-entropy and composite engineering. *Ceram. Int.* **2024**, *50*, 19488–19501. [CrossRef]
43. Chen, L.; Luo, K.R.; Li, B.H.; Hu, M.Y.; Feng, J. Mechanical property enhancements and amorphous thermal transports of ordered weberite-type RE_3Nb/TaO_7 high-entropy oxides. *J. Adv. Ceram.* **2023**, *12*, 399–413. [CrossRef]
44. Yang, J.; Li, L.; Li, C.R.; Shi, D.D.; Pan, W. Phase transformation inhibition and improved thermo-mechanical properties of rare earth niobates for thermal barrier coatings. *Ceram. Int.* **2024**, *50*, 29799–29805. [CrossRef]
45. Gan, M.D.; Lai, L.P.; Wang, J.K.; Wang, J.; Chen, L.; He, J.J.; Feng, J.; Chong, X. Suppressing the oxygen-ionic conductivity and promoting the phase stability of the high-entropy rare earth niobates via Ta substitution. *J. Mater. Sci. Technol.* **2025**, *209*, 79–94. [CrossRef]
46. Chen, L.; Wang, Y.T.; Hu, M.Y.; Zhang, L.Y.; Wang, J.K.; Zhang, Z.B.; Liang, X.B.; Guo, J.; Feng, J. Achieved limit thermal conductivity and enhancements of mechanical properties in fluorite RE_3NbO_7 via entropy engineering. *Appl. Phys. Lett.* **2021**, *118*, 071905. [CrossRef]
47. Song, G.D.; Yang, J.P.; Dong, Y.J.; Cui, C. Failure mechanism of plasma sprayed physical vapor deposition (PS-PVD) thermal barrier coating under high temperature and high velocity aviation kerosene gas thermal shock. *Corros. Prot.* **2022**, *43*, 20–25.
48. Wei, L.L.; Guo, L.; Li, M.Z.; Guo, H.B. Calcium-magnesium-alumina-silicate (CMAS) resistant Ba_2REAlO_5 (RE = Yb, Er, Dy) ceramics for thermal barrier coatings. *J. Eur. Ceram. Soc.* **2017**, *37*, 4991–5000. [CrossRef]
49. Zhang, Z.J.; Sun, J.; Liu, G.H.; Han, Y.; Liu, W.; Li, Y.; Wang, W.; Liu, X.Y.; Zhang, P.; Pan, W.; et al. High toughness and CMAS resistance of $REAlO_3/RE_2Zr_2O_7$ (RE = La, Nd, Sm, Eu, Gd, and Dy) composites with eutectic composition for thermal barrier coatings. *J. Adv. Ceram.* **2024**, *13*, 800–809. [CrossRef]
50. Li, H.Y.; Jia, Z.J.; Zhang, L.; Tian, Y.; Liu, X.G.; Bao, Y.W.; Wan, D.T. A review on the development of prestressed ceramics. *Adv. Ceram.* **2024**, *45*, 100–109.
51. Chen, L.; Hu, M.Y.; Feng, J. Mechanical properties, thermal expansion performance and intrinsic lattice thermal conductivity of $AlMO_4$ (M = Ta, Nb) ceramics for high-temperature applications. *Ceram. Int.* **2019**, *45*, 6616–6623. [CrossRef]
52. Aladdin Reagents. Available online: https://www.aladdin-e.com/zh_cn/ (accessed on 3 October 2025).
53. Bai, Y.; Han, Z.H.; Li, H.Q.; Xu, C.; Xu, Y.L.; Ding, C.H.; Yang, J.F. Structure-property differences between supersonic and conventional atmospheric plasma sprayed zirconia thermal barrier coatings. *Surf. Coat. Technol.* **2011**, *205*, 3833–3839. [CrossRef]
54. Liu, R.X.; Liang, W.P.; Miao, Q.; Zhao, H.; Zhang, X.F.; Zhang, M.; Yan, R.X.; Ramasubramanian, B.; Ramakrishna, S. Revealing the oxidation growth mechanism and crack evolution law of novel Si-$HfO_2/Yb_2Si_2O_7/Yb_2SiO_5$ environmental barrier coatings during thermal cycling. *J. Adv. Ceram.* **2024**, *13*, 1677–1696. [CrossRef]
55. Chen, L.; Wang, W.J.; Li, J.H.; Yang, G.J. Suppressing the phase-transition-induced cracking of SiO_2 TGOs by lattice solid solution. *J. Eur. Ceram. Soc.* **2023**, *43*, 3201–3215. [CrossRef]
56. Opila, E.J. Oxidation and volatilization of silica formers in water vapor. *J. Am. Ceram. Soc.* **2003**, *86*, 1238–1248. [CrossRef]
57. Parker, C.G.; Opila, E.J. Stability of the Y_2O_3-SiO_2 system in high-temperature, high-velocity water vapor. *J. Am. Ceram. Soc.* **2020**, *103*, 2715–2726. [CrossRef]
58. Schlichting, K.W.; Padture, N.P.; Klemens, P.G. Thermal conductivity of dense and porous yttria-stabilized zirconia. *J. Mater. Sci.* **2001**, *36*, 3003–3010. [CrossRef]
59. Shannon, R.D.; Prewitt, C.T. Effective ionic radii in oxides and fluorides. *Acta Cryst. B* **1969**, *25*, 925–946. [CrossRef]
60. Robinson, K.; Gibbs, G.V.; Ribbe, P.H. Quadratic elongation: A quantitative measure of distortion in coordination polyhedra. *Science* **1971**, *172*, 567–570. [CrossRef]
61. Tian, Z.L.; Lin, C.F.; Zheng, L.Y.; Sun, L.C.; Li, J.L.; Wang, J.Y. Defect-mediated multiple-enhancement of phonon scattering and decrement of thermal conductivity in $(Y_xYb_{1-x})_2SiO_5$ solid solution. *Acta Mater.* **2018**, *144*, 292–304. [CrossRef]
62. Du, Z.J.; Shan, Z.T.; Qiao, A.; Tao, H.Z.; Yue, Y.Z. Tantalum-lanthanum mixing effect on structural and mechanical properties of aluminate glasses. *J. Non-Cryst. Solids.* **2025**, *650*, 123340. [CrossRef]
63. Xie, M.X.; Xiang, C.Y.; Zeng, X.L.; Zhang, X.S.; Zhang, L.J.; Xiong, J.T. Optimization of the Raman spectroscopic method for crystal orientation and residual stress of aluminum oxide. *J. Mater. Res. Technol.* **2024**, *33*, 8265–8276. [CrossRef]

64. Spitsberg, I.; Steibel, J. Thermal and environmental barrier coatings for SiC/SiC CMCs in aircraft engine applications. *Int. J. Appl. Ceram. Technol.* **2004**, *1*, 291–301. [CrossRef]
65. Ning, D.; Huang, H.J.; Chao, R.X.; Lin, S.; Bi, Y.T. Lattice distortion, mechanical and thermodynamic properties of (TiZrHf)C and (TiZrHf)N ceramics. *Appl. Phys. A* **2023**, *129*, 720.
66. Zhang, H.; Su, J.B.; Duo, S.W.; Zhou, X.; Yuan, J.Y.; Dong, S.J.; Yang, X.; Zeng, J.Y.; Jiang, J.N.; Deng, L.H.; et al. Thermal and mechanical properties of Ta_2O_5 doped $La_2Ce_2O_7$ thermal barrier coatings prepared by atmospheric plasma spraying. *J. Eur. Ceram. Soc.* **2019**, *39*, 2379–2388. [CrossRef]
67. Zhu, S.S.; Zhu, J.P.; Ye, S.B.; Yang, K.J.; Li, M.L.; Wang, H.L.; He, J.L. High-entropy rare earth titanates with low thermal conductivity designed by lattice distortion. *J. Am. Ceram. Soc.* **2023**, *106*, 6279–6291. [CrossRef]
68. Tian, Z.L.; Zhang, J.; Zhang, T.Y.; Ren, X.M.; Hu, W.P.; Zheng, L.Y.; Wang, J.Y. Towards thermal barrier coating application for rare earth silicates RE_2SiO_5 (RE = La, Nd, Sm, Eu, and Gd). *J. Eur. Ceram. Soc.* **2019**, *39*, 1463–1476. [CrossRef]
69. Liu, X.Y.; Zhang, P.; Huang, M.Z.; Han, Y.; Xu, N.; Li, Y.; Zhang, Z.J.; Pan, W.; Wan, C.L. Effect of lattice distortion in high-entropy $RE_2Si_2O_7$ and RE_2SiO_5 (RE = Ho, Er, Y, Yb, and Sc) on their thermal conductivity: Experimental and molecular dynamic simulation study. *J. Eur. Ceram. Soc.* **2023**, *43*, 6407–6415. [CrossRef]
70. Moskal, G.; Jasik, A.; Mikuśkiewicz, M.; Jucha, S. Thermal resistance determination of $Sm_2Zr_2O_7$ + 8YSZ composite type of TBC. *Appl. Surf. Sci.* **2020**, *515*, 145998. [CrossRef]
71. Vourdas, N.; Marathoniti, E.; Pandis, P.K.; Argirusis, C.; Sourkouni, G.; Legros, C.; Mirza, S.; Stathopoulos, V.N. Evaluation of $LaAlO_3$ as top coat material for thermal barrier coatings. *Trans. Nonferrous Met. Soc. China* **2018**, *28*, 1582–1592. [CrossRef]

Disclaimer/Publisher's Note: The statements, opinions and data contained in all publications are solely those of the individual author(s) and contributor(s) and not of MDPI and/or the editor(s). MDPI and/or the editor(s) disclaim responsibility for any injury to people or property resulting from any ideas, methods, instructions or products referred to in the content.